Article

The Role of Space Charge at Metal/Oxide Interfaces in Proton Ceramic Electrochemical Cells

Sarmad W. Saeed and Tor S. Bjørheim*

Read Online

ACCESS | Metrics & More | Article Recommendations

ABSTRACT: The contact potential and the resulting charge accumulation or depletion at the electrode/electrolyte interface are investigated for Ni and Cu group metals in contact with the state-of-the-art proton conductor acceptor-doped $BaZrO_3$ by first-principles calculations and thermodynamic modeling. The contact potential depends on the metal's work function and the defect chemical properties of the oxide, rendering it strongly temperature and atmosphere dependent. Above 900 K, most metals yield negative contact potentials and enrichment of protonic charge carriers at the electrode/electrolyte interface, facilitating charge transfer. Below 600 K, the contact potentials vary from positive to negative depending on the metal's work function. As such, higher work function metals lead to a space-charge contribution to the electrode impedance at lower temperatures. The prospects of exploiting charge accumulation (or depletion) characteristics of such interfaces are furthermore discussed with a focus on nanocomposite electrodes and solid-state electrochemical capacitors.
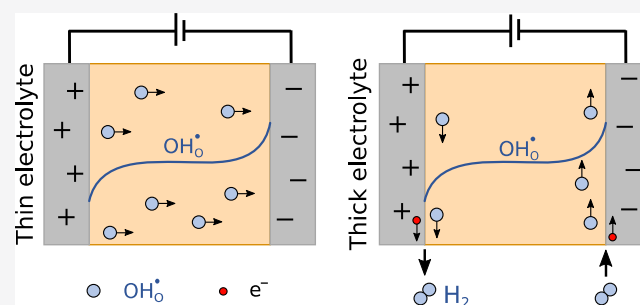
1. INTRODUCTION

Metal/oxide interfaces play an essential role in a wide range of technological applications such as electronics, heterogeneous catalysis, and energy storage and conversion devices. Metals with good catalytic and electronic transport properties, such as Ni, are widely used as negative (fuel side) electrodes in fuel cells and electrolyzers. In such applications, space-charge layers may significantly affect the overall performance of the electrode in, for instance, proton ceramic electrochemical cells (PCECs). The charge transfer between the electrolyte and the negative electrode (negatrode) involves the redox reaction at the three-phase boundary (TPB) between protons, electrons, and hydrogen, as well as the transfer of protons across the interface. The interface can be divided into the structural and the electrical interface; the former is characterized by the structural features of the interface region, while the latter is related to space-charge layers in the near-interface regions. As such, metal/electrolyte combinations that lead to space-charge depletion of charge carriers at the interface may lead to significant space-charge-associated charge transfer resistance, with similar typical double-layer capacitances.[1]

The implication of space charge at metal/oxide interfaces on the transport properties of ion conductors and interfacial mass storage has been qualitatively explored in a number of studies. For instance, Matsumoto et al.[2] reported 1 order of magnitude decrease in the electrical conductivity of acceptor-doped $SrZrO_3$ containing nanoinclusions of platinum under reducing conditions. This effect was ascribed to the formation of percolating space-charge layers with depleted charge carrier

concentration around the metal particles. Caldes et al.,[3] on the other hand, reported an increase in the electrical conductivity of acceptor-doped $BaCeO_3$ containing Ni nanoparticles and attributed that to the enhanced catalytic splitting of H_2 resulting in enrichment of $OH_O^\bullet$ near the Ni particles. Moreover, Clark et al.[4] reported enhanced proton conductivity in Y- and Yb-co-doped $BaZrO_3$ containing Ni particles. Similar results were reported by Tong et al.,[5] who studied the ionic conductivity of Y-doped $BaZrO_3$ containing Pd nanoparticles. In a computational study of the stability of protonic defects near interfaces between metals and $BaZrO_3$, Tauer et al.[6] reported favorable segregation of $OH_O^\bullet$ to the first atomic plane in $BaZrO_3$ in the case of Pt and Pd and unfavorable segregation in the case of Ag and Ni. In subsequent atomic planes, the formation energies were similar to those in the bulk. These results were supported by Malagoli et al.,[7] who performed density functional theory (DFT) calculations that pointed in the same direction. However, none of the computational studies considered how a mismatch in the electronic structure of the two joining materials affected defect segregation. Generally, metals may effectively serve as heterogeneous
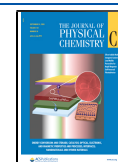
donor or acceptor phases for a solid dominated by ionic defect disorders, depending on their work function compared to the ionization potential (or rather Fermi level) of the ionic solid. Similar to the case in a metal–semiconductor contact, the metal may lead to either enhancement or depletion of ionic defects in the near-interface regions, and as such form either "resistive" or "conductive" interfaces. Furthermore, a metal that acts as a heterogeneous acceptor will lead to enrichment of positively charged defects in the ionic material and potentially enable composite electrodes with enhanced ambipolar transport properties. Understanding the role of space charge at metal/oxide interfaces will as such have large implications for the general understanding of the electrode kinetics of ionically conducting materials and also for the development of enhanced electrodes as well as potential novel applications based on mass/charge storage at metal/oxide interfaces.

In this contribution, we apply first-principles calculations and thermodynamic modeling to address the role of space charge at the interfaces between the state-of-the-art proton conductor $BaZrO_3$ and typical metals used as the negative electrode (hereafter negatrode) in ceramic electrochemical devices such as Ni, Pd, Pt, Cu, Ag, and Au. First, we explore the dependence of the interface defect chemistry on the mismatch in the electronic structure and relate the contact potential to the ionization potential of the solids. Further, we discuss the impact of space charge on the kinetics of metal electrodes and the prospect of metal/oxide interfaces as solid-state electrochemical capacitors.

2. METHODOLOGY

2.1. Bulk Thermodynamics. The total energies from DFT calculations can be used to obtain the free energy of defect formation

$$\Delta_f G_{def} = E_{def}^{el} - E_{bulk}^{el} + \Delta_f G_{def}^{vib} - \sum_i \Delta n_i \mu_i(T, p)$$
$$+ q(\varepsilon_F + \Delta\varepsilon) \tag{1}$$

where E_{def}^{el}, E_{bulk}^{el}, and $\Delta_f G_{def}^{vib}$ are the DFT energies of a defective and a perfect supercell and the vibrational contribution to the free energy, respectively. Δn_i and μ_i are the change in the number of atom type i and its chemical potential, while q, ε_F, and $\Delta\varepsilon$ are the effective charge of the defect, the Fermi level, and a correction for the shift in band edges in the calculation of charged defects arising from the addition of a jellium background, respectively. The latter is calculated from differences in the electrostatic potential of ions in the perfect and defective supercell. For small gas molecules, DFT fails in predicting the correct binding energies; therefore, we calculate the standard chemical potential of gases from the energy of isolated atoms and experimental binding energies

$$\mu_i^\circ = \sum E^{atom,DFT} + E^{binding,exp} \tag{2}$$

The chemical potential at finite temperatures and pressures are obtained from the relation

$$\mu_i = \mu_i^\circ + E_i^{ZP} + H_i^\circ(T) - TS_i^\circ(T) + k_B T \ln\left(\frac{p_i}{p^\circ}\right) \tag{3}$$

where E_i^{ZP}, $H_i^\circ(T)$, and $S_i^\circ(T)$ are the zero-point energy and temperature dependence of the standard enthalpy and entropy of gas molecule i, respectively, and are obtained from

thermodynamic tables. μ_i° is the standard chemical potential of species i.

The concentration of defects can be calculated from the free formation energy according to

$$\frac{c_i}{c_s - c_i - c_d} = \exp\left(-\frac{\Delta_f G}{k_B T}\right) \tag{4}$$

where c_i is the concentration of defect i, forming on lattice site s with concentration c_s. c_d is the concentration of all other defects that form on lattice site s. Finally, site balance is accounted for through

$$\sum_i c_i + c_{O_O^\times} = 3 \tag{5}$$

where i runs over all defects that form on the oxygen site.

2.2. Space-Charge Thermodynamics. The presence of an electrostatic potential near the interface affects the equilibrium concentration of defects, and therefore, the chemical potential has to be replaced by the electrochemical potential of defects, which reads

$$\tilde{\mu}_i = \mu_i^\circ + k_B T \ln\left(\frac{c_i(x)}{c_s - c_d(x) - c_i(x)}\right) + q_i \varphi(x) \tag{6}$$

where μ_i° is the standard chemical potential of defect i and $\varphi(x)$ is the electrostatic potential at a distance x from the interface. In the calculations, we apply the widely adopted abrupt boundary conditions in which the formation energy and other parameters change abruptly at the interface. At equilibrium, the electrochemical potential in the system is constant, such that $\tilde{\mu}_i(x) = \tilde{\mu}_{i,bulk}$, which by insertion and rearrangement gives the concentration of species i as a function of distance from the interface in terms of the electrostatic potential difference and the concentration of defects in the bulk

$$c_i(x) = \frac{(c_s - c_d(x))c_i \exp\left(-\frac{q_i \Delta\varphi(x)}{k_B T}\right)}{c_s - c_i - c_d - c_i \exp\left(-\frac{q_i \Delta\varphi(x)}{k_B T}\right)} \tag{7}$$

where $\Delta\varphi(x)$ is the electrostatic potential difference at a distance x from the interface relative to the potential in bulk. As such, the defect concentration profiles can be calculated from the electrostatic potential profile, which can be obtained from Poisson's equation

$$\frac{d^2}{dx^2}\Delta\varphi(x) = -\frac{\rho(x)}{\epsilon} \tag{8}$$

where ϵ and $\rho(x)$ are the dielectric constant and charge density, respectively. The latter is calculated from the concentration according to

$$\rho(x) = \sum_i e q_i c_i(x) \tag{9}$$

These equations are solved numerically with the following boundary conditions

$$\frac{d}{dx}\Delta\varphi(x)\bigg|_{x=\infty} = 0 \tag{10}$$

which ensures that the electrostatic potential in the bulk is constant, and
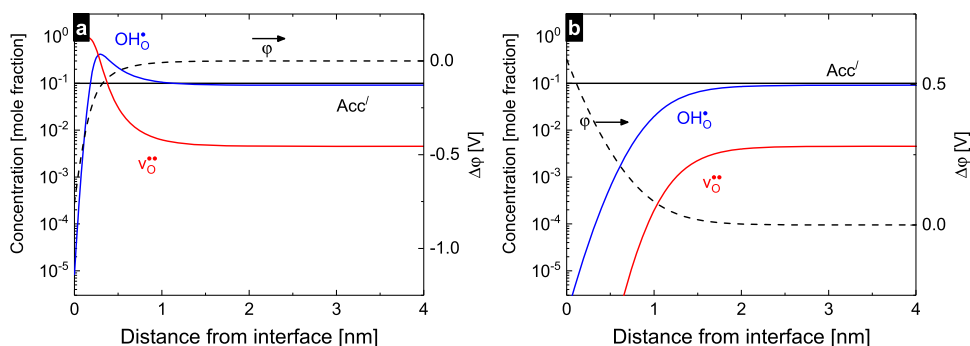
Figure 1. Electrostatic potential and defect concentration profiles in $BaZrO_3$ in contact with (a) Pt and (b) Ag as a function of distance from the interface at 600 K under wet, reducing conditions ($p_{H_2O} = 0.03$ atm and $p_{O_2} = 10^{-30}$ atm). The profiles are calculated according to the Mott–Schottky model.

$$\frac{d}{dx}\Delta\varphi(x) = \Delta\varphi_0\bigg|_{x=0} \quad (11)$$

$\Delta\varphi_0$ in eq 10 is the electrostatic potential at the interface relative to that in the bulk of $BaZrO_3$. At the metal side, the change in the electrostatic potential is negligibly low as a consequence of the high concentration of electrons. $\Delta\varphi_0$ is obtained from the segregation energy of a charged species utilizing an indirect interface model, as described in refs 8, 9, in which we consider the isolated systems and align the resulting defect energetics with respect to the vacuum level

$$\Delta\varphi_0 = \frac{1}{q_i}\left[(\Delta\mu^{seg}) + k_B T \ln\left(\frac{c'_{i,bulk}[c_s - c_{i,bulk}]}{c_{i,bulk}[c'_s - c'_{i,bulk}]}\right)\right] \quad (12)$$

where c_i and c'_i are the concentrations of species i in the two phases. $\Delta\mu^{seg}$ is the difference in the standard chemical potential of species i in the two phases after alignment with respect to the vacuum level, that is, by replacing ε_F in eq 1 with the ionization potential of the perfect solid. $\Delta\varphi_0$ may also be obtained directly as the difference in the aligned Fermi levels of the metal and the doped oxide.

The chemical capacitance that results from the polarization of the space-charge layer is calculated from the relation

$$C = \frac{dQ_{rel}}{dV} \quad (13)$$

where V is the applied voltage and Q_{rel} is the excess charge that is stored in response to the external potential and is given by

$$Q_{rel} = Q_V - Q_{V=0} = \int_0^{x_b} \rho(x)dx\bigg|_V - \int_0^{x_b} \rho(x)dx\bigg|_{V=0} \quad (14)$$

The energy stored in the capacitor is obtained by integrating the voltage with respect to charge

$$E = \int_0^{Q_{rel}} V(q)dq \quad (15)$$

2.3. DFT Calculations. All first-principles calculations were performed using the plane-wave DFT with the generalized gradient approximation of Perdew, Burke, and Ernzerhof (GGA-PBE)[10] functional as implemented in the Vienna ab initio simulation (VASP) code.[11−13] Projector augmented wave (PAW) potentials[14,15] with valence configurations $5s^25p^66s^2$, $4s^24p^64d^25s^2$, $2s^22p^4$, $3d^84s^2$, $4d^{10}$, $5d^96s^1$, $3d^{10}4s^1$, $4d^{10}5s^1$, and $5d^{10}6s^1$ for Ba, Zr, O, Ni, Pd, Pt, Cu, Ag, and Au,

respectively, were used. A constant cutoff energy of 500 eV and convergence criteria of 10^{-4} and 10^{-8} eV, respectively, for the ionic and electronic relaxations, were employed. A $3 \times 3 \times 3$ supercell of cubic ($Pm\bar{3}m$) $BaZrO_3$ has been used for total energy calculations, using a $2 \times 2 \times 2$ k-mesh that has been sampled according to the Monkhorst–Pack scheme. For the calculation of vacuum potentials, $1 \times 1 \times 11$ supercells with a k-mesh of $6 \times 6 \times 1$ were used. Slab calculations on $BaZrO_3$ were performed on the ZrO_2-terminated surface with 11 atom layers. Slab calculations on the metals were performed on 13 atom layers. In both types of slabs, a vacuum layer of at least 25 Å was used. The vibrational formation entropies and zero-point energies were calculated with the finite displacement method as implemented in the phonopy code,[16] using displacements of ± 0.01 Å, and evaluated at the Γ-point.

3. RESULTS AND DISCUSSION

3.1. Interface Defect Chemistry. In line with experimental[17−19] and previous computational[20,21] studies, the calculated defect structure of acceptor-doped $BaZrO_3$ is dominated by $OH_O^\bullet$ below 850 K, above which $v_O^{\bullet\bullet}$ becomes the dominating charge compensating defect in wet reducing or oxidizing atmospheres (Figure 1). In addition, electron holes, which dominate the electrical conductivity of $BaZrO_3$ at high temperature and oxygen partial pressure due to their high mobility, exhibit a negligibly low concentration[22] and are therefore omitted. It should be noted that the concentration profile of electron holes exhibits the same behavior as that of $OH_O^\bullet$ close to an interface. Further, the calculated concentration of v_{Ba}'' is substantially higher than that of v_{Zr}''' but the concentration of both defects is predicted to be insignificant compared to the acceptor concentration in the considered temperature range. As such, the defect chemistry of metal/$BaZrO_3$ interfaces is mainly governed by $OH_O^\bullet$ and $v_O^{\bullet\bullet}$.

Figure 1 shows the calculated concentration and electrostatic potential profiles near the interfaces between $BaZrO_3$ and Pt or Ag at 600 K. The profiles are calculated in the Mott–Schottky limit, assuming a constant dopant concentration up to the interface, which represents the situation in samples synthesized at low temperature, for instance, by pulsed laser deposition (PLD). For the Pt interface, the difference in electrostatic potential with respect to the bulk part of $BaZrO_3$, $\Delta\varphi$, is −0.76 V, which thus results in enrichment of positively charged defects at the $BaZrO_3$ side of the interface. Towards the interface, the concentration of the minority $v_O^{\bullet\bullet}$ increases and eventually approaches unity due to their double charge.
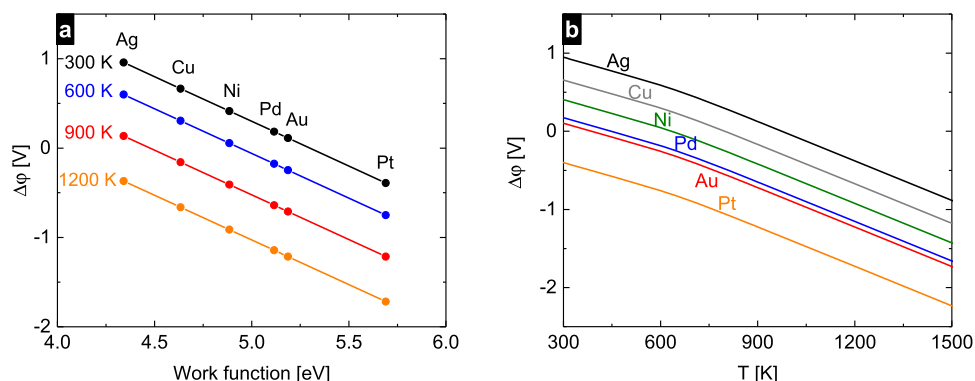
Figure 2. Electrostatic potential difference between the interface and bulk $BaZrO_3$ as a function of metal work function (a) and as a function of temperature (b) under wet, reducing conditions ($p_{H_2O} = 0.03$ atm and $p_{O_2} = 10^{-30}$ atm) for a number of metals that are typically used as electrodes or current collectors in electrochemical applications.

Consequently, $OH_O^\bullet$ is enriched in the low-potential parts of the space-charge region but is depleted closer to the interface plane as a result of the competition with $v_O^{\bullet\bullet}$, which forms on the same lattice site. Although $OH_O^\bullet$ predominates in the bulk, most of the charge accumulation in the 1 nm wide space-charge layer is due to $v_O^{\bullet\bullet}$ (1.14 of 1.32 C/m^2). In the case of Ag, however, $\Delta\varphi$ is 0.59 V at 600 K, which thus causes a depletion of $OH_O^\bullet$ and $v_O^{\bullet\bullet}$ in the near-interface region of $BaZrO_3$. The concentrations of $OH_O^\bullet$ and $v_O^{\bullet\bullet}$ are ~5 and ~11 orders of magnitude lower at the interface plane than those in the bulk. Moreover, the space-charge layer width is larger compared to that at the Pt/$BaZrO_3$ contact, which is due to the limited number of sites (i.e., defects) that can be depleted.

The large change in $\Delta\varphi$ upon the replacement of Pt with Ag reflects the strong dependence of $\Delta\varphi$ on the choice of metal. Figure 2a displays $\Delta\varphi$ as a function of the metal work function for common metals at selected temperatures, indicating a linear dependence of $\Delta\varphi$ on the work function of the metal. This trend is in line with the Schottky barrier height at metal/semiconductor interfaces.[23,24] However, as with metal/semiconductor interfaces, deviations from the predicted trend are to be expected as a consequence of possible segregation of defects to the interface plane, which thus acts in a similar manner as the metal-induced gap states at metal/semiconductor interfaces.[25] For several of the interfaces considered here, the segregation energy of, for instance, protons is weakly (un)favorable and minute compared to the electrostatic potential difference arising from the difference in electronic structure between the metal and the oxide.[6,7] Due to its minor effect on the defect chemistry of the considered interfaces, such segregation will not be further addressed. Figure 2b shows the calculated $\Delta\varphi$ as a function of temperature. $\Delta\varphi$ exhibits two linear regions, one at low and one at high temperature with slopes of −1.2 and −1.7 mV/K, respectively, and a transition region between 600 and 900 K, which corresponds to the transition from $OH_O^\bullet$ to $v_O^{\bullet\bullet}$ dominated defect structure of $BaZrO_3$. This shows that $\Delta\varphi$ is dependent on external parameters (such as p_{H_2O} or p_{O_2}) that affect the defect chemistry of bulk $BaZrO_3$. At 300 K, $\Delta\varphi$ is positive for all metals (except for Pt) and decreases with increasing temperature, eventually taking on negative values at the highest temperatures. At typical operating temperatures of proton ceramic electrochemical cells (700−1000 K), Au, Pt, Pd, Ni, and Cu lead to small or negative $\Delta\varphi$ and as such a defect enrichment layer at the contact with $BaZrO_3$. This is in

line with the reported increase in ionic conductivity of composites between metals (Pd or Ni) and oxides.[3−5]

3.2. Space-Charge and Metal Electrode Properties. The performance of an electrode relies on the kinetics of several individual steps that involve gas diffusion, adsorption, and dissociation on the electrode surface, subsequent bulk or surface diffusion to and from the electrode/electrolyte interface, and oxidation (or reduction) and H$^+$ transfer between the negatrode and the electrolyte. In terms of proton ceramic electrochemical cells (PCECs), the latter steps constitute the charge transfer resistance, which involves migration of H$^+$ to (or from) the electrode/electrolyte interface and is as such affected by the presence of a charge-depletion or enrichment layer at the electrode/electrolyte interface. Previous studies on oxide/oxide interfaces in which the individual materials are dominated by electrons and ionic defects as charge-compensating defects show that such interfaces exhibit a depletion layer at the interface where the concentrations of electrons and ionic charge carriers are reduced by several orders of magnitude.[8] Figures 1b and 2 show that Ag, Cu, and Ni, which exhibit the highest contact potentials, result in charge carrier depletion in the space-charge region of the electrolyte similar to that at interfaces between acceptor-doped and donor-doped oxides. Consequently, this would result in a higher charge transfer resistance at low temperatures due to the more positive $\Delta\varphi$. As such, the electrode kinetics of these metals may be limited by charge-carrier migration through the space-charge layer. In terms of electrolysis, when the negatrode is in cathodic operation, a depletion layer would lower the current density and consequently require large overpotential to suppress the depletion of charge carriers, which thus decreases the conversion efficiency. Indeed, a metal that results in negative $\Delta\varphi$ would be more suitable as an electrode, since it results in enrichment of charge carriers, and thus reduces the resistance. However, as Figure 1a shows, too negative $\Delta\varphi$ results in enrichment of $v_O^{\bullet\bullet}$ at the expense of the concentration of $OH_O^\bullet$ close to the phase boundary, which consequently increases the electrode resistance. As such, in addition to good catalytic properties, a metal electrode should exhibit small, negative $\Delta\varphi$ at the operating temperature.

Our results suggest that the charge transfer resistance is not limited by diffusion across the space-charge layer at higher temperatures. This conclusion is in line with experiments where measurements on Pt and Cu electrodes indicate that the
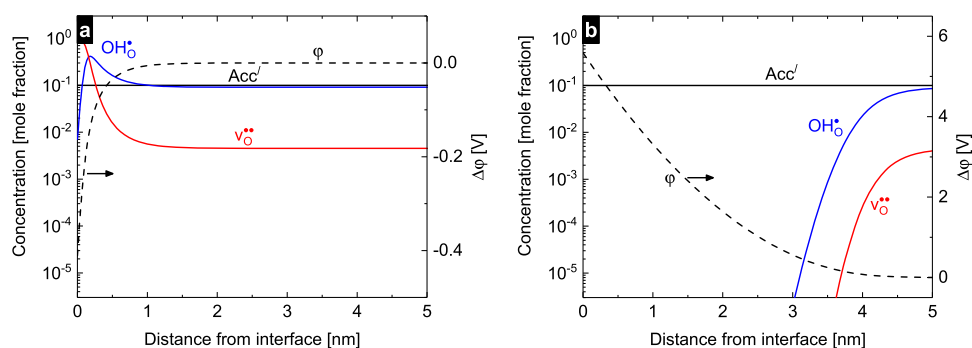
Figure 3. Electrostatic potential and defect concentration profiles in BaZrO$_3$ as a function of distance from the interface under applied biases of −1 V (a) and 5 V (b) at 600 K. The profile under no bias is shown in Figure 1b.
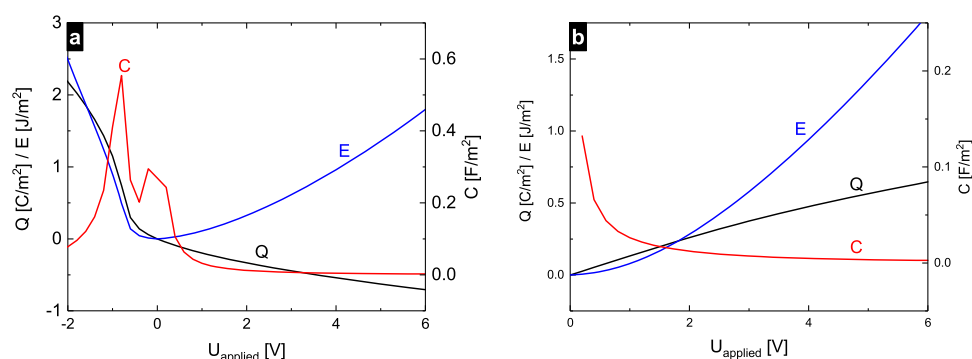

Figure 4. Charge (relative to under 0 applied voltage) near the interface between BaZrO$_3$ and Ag, chemical capacitance, and area-specific energy density as a function of the applied voltage for a single interface (a) and for a parallel-plate capacitor (i.e., two interfaces in series; Ag/BaZrO$_3$/Ag) (b).

availability of atomic hydrogen and hydrogen oxidation, respectively, are the limiting steps for these electrodes.[26]

Besides enhancing the performance of the electrode, enrichment of OH$_O^\bullet$ near the interface can result in job-sharing storage of H$_2$, in which H$_2$ is stored as H$^+$ on the oxide side of the interface and e$^-$ in the metal. Job-sharing storage of H$_2$ in composites of metals and oxides has previously been confirmed experimentally in the composites of Li$_2$O and Ru.[27]

3.3. Bias Dependence and Chemical Capacitance. The application of an electric potential affects $\Delta\varphi$ and may, as such, significantly influence the space-charge characteristics. Figure 3 shows the equilibrium defect concentration and potential profiles under the application of potentials of −1 and 5 V at the interface between Ag and BaZrO$_3$. In this context, a positive potential (or bias) corresponds to increasing $\Delta\varphi$, while a negative potential corresponds to decreasing it. Applying a bias of −1 V causes enrichment of defects and increases the charge stored near the interface by 1.15 C/m^2 to a total of 0.87 C/m^2 at the same time as the space-charge layer width is reduced compared to under no bias (1 nm vs 2 nm). On the other hand, a bias of 5 V further depletes the interface charge by 0.63 C/m^2 to a total of −0.91 C/m^2 and results in a much wider space-charge layer (4 nm) as a consequence of the limited number of sites/defects that can be depleted.

The large intrinsic polarization at metal/BaZrO$_3$ interfaces suggests that solid ion conductors may be suitable as electrolytes in supercapacitors. The charge, capacitance, and stored energy as a function of applied potential for a single Ag/BaZrO$_3$ interface are shown in Figure 4a. The resulting capacitance exceeds 240 μF/cm^2 (depending on the direction and magnitude of the applied potential), which is comparable to the capacitances of the best supercapacitors applying RuO$_2$-coated electrodes (where the reduction of RuO$_2$ gives capacitances of up to 200 μF/cm^2).[28] The saddle shape around −0.59 V occurs due to the cancellation of the contact potential, which is +0.59 V, that is, at this voltage, there is no space charge in BaZrO$_3$. Hence, a small change in the applied potential results in a substantial amount of charge at the interface and thereby large capacitance.

Figure 4b shows the charge, capacitance, and energy density as a function of the applied voltage for a parallel-plate capacitor, consisting of acceptor-doped BaZrO$_3$ and Ag electrodes. The curves are similar to those on the positive side of the x-axis of Figure 4a, reflecting that the properties of such a capacitor are limited by the positive electrode, where the difficulty of depleting charge requires a large potential drop. Thus, the resulting capacitance is lower than the maximum value of the single interfaces. However, as with traditional supercapacitors, the use of asymmetric electrodes can be exploited to improve the total capacitance and energy density.

Despite similar capacitances, there are fundamental differences between a liquid and a solid electrolyte supercapacitor. In a liquid electrolyte, the concentration of charge carriers is low; however, since both cations and anions are mobile, ions in the entire electrolyte contribute during charging, such that the electrolyte center is depleted for charge carriers. In solid electrolytes, usually, one or more species are effectively immobile, such as the cationic acceptors in BaZrO$_3$, with the consequence that the concentration of mobile defects remains constant in the center of the electrolyte during charging, to maintain electroneutrality. Thus, the polarization near the

electrodes corresponds to moving charge carriers from one side of the electrolyte to the other. For thinner electrolytes, this process is fast; however, for thicker ones, reactions at the TPB (as illustrated in Figure 5) may provide a faster charging alternative.
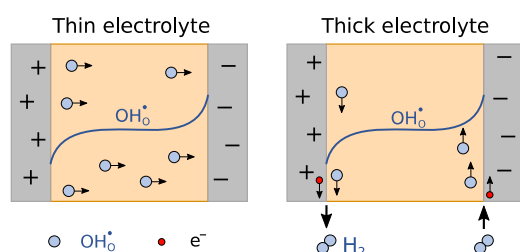

Figure 5. Schematic illustration of how a capacitor may charge in the limits of very thin or very thick electrolyte. The solid line shows the $OH_O^\bullet$ concentration profile within the electrolyte.

Ceramic electrolytes can withstand high voltages (close to or even higher than the bandgap), which is beneficial in terms of energy capacity, as the stored energy scales with the square of the applied voltage. For instance, supercapacitors with aqueous electrolytes exhibit higher capacitances than the ones applying organic electrolytes; however, the latter exhibits higher energy density due to operating at higher voltages (up to 2.7 V vs 1.0 V for the former).[28] Moreover, solid electrolytes have several benefits compared to traditional supercapacitors in terms of thermal stability and evaporation or leakage of the liquid electrolyte, which are typical issues with the latter. In addition, the possibility of using thinner electrolytes may result in shorter charging time and enhanced energy density.

4. CONCLUSIONS

The space-charge properties of the interfaces between the Ni and Cu group metals and proton-conducting $BaZrO_3$ have been studied by first-principles calculations. It was found that the electrostatic potential at the interfaces, $\Delta\varphi$, is negative for most considered metals at the typical operating temperature of proton ceramic cells and decreases with increasing temperature. Furthermore, $\Delta\varphi$ correlates with the work function of the metal, showing a linear decrease with increasing work function. In terms of electrodes for proton ceramic cells, our calculations show that diffusion across the space-charge region is not a limiting factor for the charge transfer resistance at the highest operating temperatures due to enrichment of charge carriers at the electrode–electrolyte interface. Finally, space-charge formation results in large area-specific chemical capacitances that exceed 240 $\mu F/m^2$, which in combination with the possibility of operating at high voltages show that proton-conducting oxides may be suitable as electrolytes in high energy density solid-state capacitors.

■ AUTHOR INFORMATION

Corresponding Author

Tor S. Bjørheim − *Centre for Materials Science and Nanotechnology, Department of Chemistry, University of Oslo, NO-0349 Oslo, Norway;* ● orcid.org/0000-0002-5720-2784; Email: torsb@kjemi.uio.no

Author

Sarmad W. Saeed − *Centre for Materials Science and Nanotechnology, Department of Chemistry, University of Oslo, NO-0349 Oslo, Norway;* ● orcid.org/0000-0002-5234-8573

Complete contact information is available at:
https://pubs.acs.org/10.1021/acs.jpcc.0c07228

Notes

The authors declare no competing financial interest.

■ ACKNOWLEDGMENTS

■ REFERENCES

(1) Jamnik, J.; Maier, J.; Pejovnik, S. Interfaces in Solid Ionic Conductors: Equilibrium and Small Signal Picture. *Solid State Ionics* **1995**, *75*, 51−58.

(2) Matsumoto, H.; Tanji, T.; Amezawa, K.; Kawada, T.; Uchimoto, Y.; Furuya, Y.; Sakai, T.; Matsuka, M.; Ishihara, T. Nanoprotonics in Perovsikte-Type Oxides: Reversible Changes in Color and Ion Conductivity due to Nanoionics Phenomenon in Platinum-Containing Perovskite Oxide. *Solid State Ionics* **2011**, *182*, 13−18.

(3) Caldes, M. T.; Kravchyk, K. V.; Benamira, M.; Besnard, N.; Gunes, V.; Bohnke, O.; Joubert, O. Metallic Nanoparticles and Proton Conductivity: Improving Proton Conductivity of $BaCe_{0.9}Y_{0.1}O_{3-\delta}$ Using a Catalytic Approach. *Chem. Mater.* **2012**, *24*, 4641−4646.

(4) Clark, D.; Tong, J.; Morrissey, A.; Almansoori, A.; Reimanis, I.; O'Hayre, R. Anomalous Low-Temperature Proton Conductivity Enhancement in a Novel Protonic Nanocomposite. *Phys. Chem. Chem. Phys.* **2014**, *16*, 5076−5080.

(5) Tong, J.; Subramaniyan, A.; Guthrey, H.; Clark, D.; Gorman, B. P.; O'Hayre, R. Electrical Conductivities of Nano Ionic Composite Based on Yttrium-Doped Barium Zirconate and Palladium Metal. *Solid State Ionics* **2012**, *211*, 26−33.

(6) Tauer, T.; O'Hayre, R.; Medlin, J. W. An ab Initio Investigation of Proton Stability at $BaZrO_3$ Interfaces. *Chem. Mater.* **2014**, *26*, 4915−4924.

(7) Malagoli, M.; Liu, M. L.; Park, H. C.; Bongiorno, A. Protons Crossing Triple Phase Boundaries Based on a Metal Catalyst, Pd or Ni, and Barium Zirconate. *Phys. Chem. Chem. Phys.* **2013**, *15*, 12525.

(8) Saeed, S. W.; Norby, T.; Bjørheim, T. S. Charge-Carrier Enrichment at $BaZrO_3/SrTiO_3$ Interfaces. *J. Phys. Chem. C* **2019**, *123*, 20808−20816.

(9) Saeed, S. W.; Norby, T.; Bjørheim, T. S. First-Principles Analyses of Nanoionic Effects at Oxide−Oxide Heterointerfaces for Electrochemical Applications. *J. Phys. Chem. C* **2020**, *124*, 14072−14081.

(10) Perdew, J. P.; Burke, K.; Ernzerhof, M. Generalized Gradient Approximation Made Simple. *Phys. Rev. Lett.* **1996**, *77*, No. 3865.

(11) Kresse, G.; Hafner, J. Ab Initio Molecular-Dynamics Simulation of the Liquid-Metal–Amorphous-Semiconductor Transition in Germanium. *Phys. Rev. B* **1994**, *49*, No. 14251.

(12) Kresse, G.; Furthmüller, J. Efficiency of Ab-Initio Total Energy Calculations for Metals and Semiconductors Using a Plane-Wave Basis Set. *Comput. Mater. Sci.* **1996**, *6*, 15−50.

(13) Kresse, G.; Furthmüller, J. Efficient Iterative Schemes for Ab Initio Total-Eergy Calculations Using a Plane-Wave Basis Set. *Phys. Rev. B* **1996**, *54*, No. 11169.

(14) Blöchl, P. E. Projector Augmented-Wave Method. *Phys. Rev. B* **1994**, *50*, No. 17953.

(15) Kresse, G.; Joubert, D. From Ultrasoft Pseudopotentials to the Projector Augmented-Wave Method. *Phys. Rev. B* **1999**, *59*, No. 1758.

(16) Togo, A.; Tanaka, I. First Principles Phonon Calculations in Materials Science. *Scr. Mater.* **2015**, *108*, 1−5.

(17) Kreuer, K. D. Aspects of the Formation and Mobility of Protonic Charge Carriers and the Stability of Perovskite-Type Oxides. *Solid State Ionics* **1999**, *125*, 285−302.

(18) Schober, T.; Bohn, H. G. Water Vapor Solubility and Electrochemical Characterization of the High Temperature Proton Conductor $BaZr_{0.9}Y_{0.1}O_{2.95}$. *Solid State Ionics* **2000**, *127*, 351−360.

(19) Kjølseth, C.; Wang, L.-Y.; Haugsrud, R.; Norby, T. Determination of the Enthalpy of Hydration of Oxygen Vacancies in Y-Doped $BaZrO_3$ and $BaCeO_3$ by TG-DSC. *Solid State Ionics* **2010**, *181*, 1740−1745.

(20) Bjørheim, T. S.; Kuwabara, A.; Ahmed, I.; Haugsrud, R.; Stølen, S.; Norby, T. A Combined Conductivity and DFT Study of Protons in $PbZrO_3$ and Alkaline Earth Zirconate Perovskites. *Solid State Ionics* **2010**, *181*, 130−137.

(21) Bjørheim, T. S.; Kotomin, E. A.; Maier, J. Hydration Entropy of $BaZrO_3$ from First Principles Phonon Calculations. *J. Mater. Chem. A* **2015**, *3*, 7639−7648.

(22) Bohn, H. G.; Schober, T. Electrical Conductivity of the High-Temperature Proton Conductor $BaZr_{0.9}Y_{0.1}O_{2.95}$. *J. Am. Ceram. Soc.* **2000**, *83*, 768−772.

(23) Freeouf, J. L.; Woodall, J. M. Schottky Barriers: An Effective Work Function Model. *Appl. Phys. Lett.* **1981**, *39*, 727−729.

(24) Tung, R. T. Schottky Barrier Height—Do We Really Understand What We Measure? *J. Vacuum Sci. Technol., B* **1993**, *11*, 1546−1552.

(25) Bardeen, J. Surface States and Rectification at a Metal Semi-Conductor Contact. *Phys. Rev.* **1947**, *71*, No. 717.

(26) Robinson, S.; Kjølseth, C.; Norby, T. Comparison of Cu and Pt Point-Contact Electrodes on Proton Conducting $BaZr_{0.7}Ce_{0.2}Y_{0.1}O_{3−\delta}$. *Solid State Ionics* **2017**, *306*, 38−47.

(27) Fu, L.; Tang, K.; Oh, H.; Manickam, K.; Bräuniger, T.; Chandran, C. V.; Menzel, A.; Hirscher, M.; Samuelis, D.; Maier, J. "Job-Sharing" Storage of Hydrogen in Ru/Li_2O Nanocomposites. *Nano Lett.* **2015**, *15*, 4170−4175.

(28) Winter, M.; Brodd, R. J. What Are Batteries, Fuel Cells, and Supercapacitors? *Chem. Rev.* **2004**, *104*, 4245−4270.